Analytical Analysis of Quasi-Halbach Array Permanent-Magnet Motors Based on Field Separation Theory

Zhaokai Li, *Member, IEEE*, Zhuo Chen, *Graduate Student Member, IEEE*, Yiming Shen, *Member, IEEE*, Ye Ma, Xiaoyan Huang, *Member, IEEE*, and Luca Peretti, *Senior Member, IEEE*

***Abstract*—This paper proposes the field separation theory for predicting the magnetic field of a quasi-Halbach array permanent-magnet motor considering the magnetization pattern and iron saturation. According to the proposed method, the air-gap field consists of a permanent-magnet field, winding current field, and equivalent saturation field. The equivalent permanent-magnet currents replacing the Halbach array with radial or parallel magnetization are introduced to obtain the linear analytical air-gap field of the permanent magnets. The winding current field relating to the slot shape and air-gap length can be directly determined using the linear analytical model. The equivalent saturation field is derived from the combination of the linear analytical model in the air gap and the magnetic circuit model in the iron region. The finite-element analysis of an 8-pole/9-slot Halbach array permanent-magnet motor and its prototype experiments are carried out to verify the effectiveness of the field separation theory, which is then used to analyze the harmonic magnetic field of Halbach array permanent-magnet motors to further improve the electromagnetic torque estimation.**

***Index Terms*—Field separation theory, analytical model, magnetization pattern, quasi-Halbach array permanent-magnet motor.**

I. Introduction

THE quasi-Halbach array permanent-magnet synchronous motors (QHAPMSM) have an outstanding ability to enhance the fundamental amplitude of air-gap field while removing the rotor iron. Therefore, it can exhibit the feature of high torque density and has been widely used in electric aircraft [1], spacecraft applications [2], and hybrid vehicles [3]. There are intense demands to design and optimize the QHAPMSM with high calculation accuracy and efficiency while keeping high insight towards improving the motor performance.

Generally, the finite-element method (FEM) achieves the highest accuracy in predicting the performance of different kinds of permanent magnet motors, but it requires the large computational resource [4]-[7]. Therefore, the optimization method is essential to obtain the best design case. Chen *et al.* employed sensitivity analysis and response surface analysis using FEM to select the key parameters and construct the optimization algorithm for the design of the permanent-magnet (PM) motors with Halbach array [8]. Xu *et al.* focused on the variable working conditions for oceanic application and conducted the multiple objective optimization of linear-rotary generator with Halbach PM array to reach maximum power generation [9]. However, these optimization methods in [8]-[9] make it difficult to find the internal relationship between motor performance and motor dimension.

A simple magnetic circuit model was built and solved using Levenberg–Marquardt algorithm for the Halbach array PM motor in [10] considering iron saturation. Still, the calculation accuracy cannot be guaranteed if the mesh of magnetic reluctance is coarse or inappropriate. In [11], the limited angle torque motor with Halbach array PM was fully parameterized using the flexible equivalent magnetic circuit. The multiple objective particle swarm optimization was used to obtain the Pareto front. It can be seen that the magnetic circuit model cannot give a clear expression of the motor performance due to the large permeance matrix, making it more similar to FEM. Hence, the advantage of the magnetic circuit model is insignificant compared with FEM.

The analytical model based on Poisson/Laplace equation can rapidly predict either slotless [1]-[2], [12]-[13] or slotted Halbach array PM motors [14]-[16]. However, the iron saturation was neglected in [1]-[2], [12]-[15], which can significantly decrease the calculation accuracy for motors with saturated iron. The method in [16] required prior knowledge of the permeability in the stator tooth body and tip, making it impractical for motor design. Meanwhile, the number of PM segments and the magnetization pattern were analytically investigated for the Halbach array PM motors in [1] and [12], respectively. The slotting effect of the Halbach array PM motors can be represented using the relative permeance function in [14]-[15] or the subdomain technique in [16]. Miroslav *et al.* presented the whole optimization design process using the analytical model [13]. To further improve the analytical model for Halbach array PM motors, it is necessary to account for the iron saturation in the calculation of motor performance, which is one of the key contributions in this paper.

There are a few works of literature about the improved analytical model for predicting the performance of surface-mounted PM motors [17]-[18], interior PM motors [19]-[21], axial-flux PM motors [22], and vernier PM motors [23]-[29]. However, for these kinds of motors [17]-[29], the permeability of rotor iron is either assumed or transformed to be infinite to

This work was supported in part by the National Key R&D Program of China (2019YFE0123500), in part by the Zhejiang Provincial Ten-Thousand-Talent Plan under Grant (2019R52003), and in part by the Zhejiang Provincial Natural Science Foundation of China under Grant No. LQ22E070003. (Corresponding author: Zhuo Chen and Xiaoyan Huang)

Zhaokai Li and Luca Peretti are with Department of Electrical Engineering, KTH Royal Institute of Technology, Stockholm, 11428 Stockholm, Sweden. (e-mail: zhaokai@kth.se; lucap@kth.se)

Zhuo Chen, Ye Ma, and Xiaoyan Huang are with Zhejiang Provincial Key Laboratory of Electrical Machine Systems, College of Electrical Engineering, Zhejiang University, 310027 Hangzhou, China. (e-mail: z.chen@zju.edu.cn; maye1998@zju.edu.cn; xiaoyanhuang@zju.edu.cn)

Yiming Shen is with the School of Electrical and Electronic Engineering, Nanyang Technological University, Singapore, 639798 (e-mail: yiming.shen@ntu.edu.sg)

satisfy the boundary condition in the analytical model. In [28], the iron saturation of the flux reversal motor with Halbach array PMs was represented using the modification of air-gap permeability and then the motor performance was analytically calculated. However, it only considers radial magnetization pattern, which means the auxiliary magnets in Halbach array PMs are tangentially magnetized, which is difficult to manufacture in industrial applications. In [29], the open-circuit air-gap field of the interior PM motor was obtained from the equivalent current on the rotor surface rather than the surface current for PMs, which made it difficult to separate the PM field from the total magnetic field and analyze the influence of different components of the total air-gap field on the motor performance.

This paper proposed the field separation theory (FST) to analyze the performance of QHAPMSM considering both slotting effect and iron saturation. The surface current of PMs is generalized to represent different magnetization patterns in either polar or Cartesian coordinates so that it is capable for all Halbach array PM motors, which has never been reported in the literature. Furthermore, as the non-magnetic rotor (only shaft and PMs) is common in Halbach array PM motors, the FST is capable of representing such differences from the rotor with electrical steel. But this feature is often neglected in other literature about analytical models of PM motors. Last but not least, the FST combines the linear analytical model (LAM) with the magnetic circuit model to predict the PM field, winding current field, and equivalent saturation field separately and analytically. Both FEM and experimental results validate the accuracy of FST. When investigating the QHAPMSM using FST, the influence of magnetization pattern on the electromagnetic torque can be quantitatively presented, which will help to improve the motor performance further.

II. Field Separation Theory

The FST has the following assumptions: a) The PMs have linear magnetization, and their relative permeability equals one; b) The end effect and eddy current effect of the QHAPMSM are neglected; c) The iron, copper, and PM materials are isotropic and homogenous.

A. Linear Analytical Model for Halbach PM Array and Winding Current

In the LAM, the equivalent currents are introduced to represent the PMs and winding currents. The value and the position of these currents are the keys to obtaining the analytical air-gap field first considering different magnetization patterns. Fig. 1 shows that the PMs with radial and tangential magnetization are replaced by the surface current along the PM sides i_{PM_r} and the inner or outer surface of PM i_{PM_t}, respectively. The fundamental theory for this transformation is the superposition of two vectors in the radial and tangential directions. Their values are calculated using

$$i_{PM\_r}(r_{PM},\alpha_{PM1}) = i_{PM\_r}(r_{PM},\alpha_{PM2}) = \frac{H_{cj}h_m}{n_{PM\_r}} \quad (1)$$

$$i_{PM\_t}(R_r,\alpha_{PM}) = i_{PM\_t}(R_m,\alpha_{PM}) = \frac{H_{cj}R_r\alpha_0}{n_{PM\_t}} \quad (2)$$

where H_{cj}, h_m, R_r, R_m, and α_0 are the coercivity, height, inner radius, outer radius and pole-arc angle of PM. n_{PM_t} and n_{PM_t} are the numbers of surface PM current in the radial and tangential direction. r_{PM} is the distance between the position of i_{PM_r} and the motor center. α_{PM} is the angle for the position of i_{PM_t} in the polar coordinate. They are also defined in Fig. 1. $R_r \le r_{PM} \le R_m$ and $\alpha_{PM1} \le \alpha_{PM} \le \alpha_{PM2}$, where α_{PM1} and α_{PM1} are the angles of both sides in each magnet.

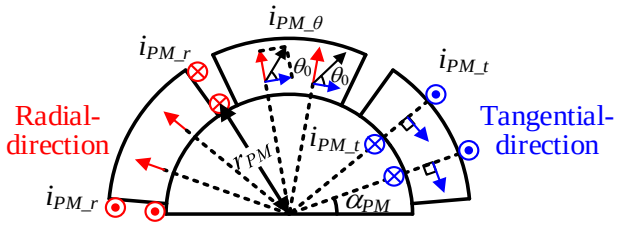

Fig. 1 The equivalence between surface current and Halbach PM array in the polar coordinate.

Then, the Halbach PM array with different magnetization directions based on polar coordinate can be represented by combining the surface current of PMs with radial and tangential magnetization using the vector synthesis method (see the black arrows in Fig. 1). The positions of the surface current stay unchanged while their values are obtained as

$$i_{PM\_\theta}(r_{PM},\alpha_{PM1}) = i_{PM\_\theta}(r_{PM},\alpha_{PM2}) = \frac{H_{cj}h_m}{n_{PM\_r}}\sin(\theta_0) \quad (3)$$

$$i_{PM\_\theta}(R_r,\alpha_{PM}) = i_{PM\_\theta}(R_m,\alpha_{PM}) = \frac{H_{cj}R_r\alpha_0}{n_{PM\_t}}\cos(\theta_0) \quad (4)$$

where θ_0 is the angle between the real magnetization direction and tangential direction. It is noted that there is no air gap between the primary and auxiliary magnets, as is not emphasized in Fig. 1.

As for the Halbach PM array with parallel magnetization based on the Cartesian coordinate in Fig. 2, the surface currents are divided into two parts to represent the parallel magnetization pattern in two directions. For X-direction, the surface currents along both sides of PM i_{PM_x1} produce the radial magnetization, as expressed in (5). Meanwhile, it is corrected by adding the surface current on the inner and outer surface of PM. According to the vector synthesis method, the value of surface PM current i_{PM_x2} is calculated using

$$i_{PM\_x1}(r_{PM},\alpha_{PM1}) = i_{PM\_x1}(r_{PM},\alpha_{PM2}) = \frac{H_{cj}h_m}{n_{PM\_r}}\cos\left(\frac{\alpha_0}{2}\right) \quad (5)$$

$$i_{PM\_x2}(R_r,\alpha_{PM}) = i_{PM\_x2}(R_m,\alpha_{PM}) = \frac{H_{cj}R_r\alpha_0}{n_{PM\_t}}\sin\left(\alpha_{PM} - \frac{\alpha_{PM1}+\alpha_{PM2}}{2}\right) \quad (6)$$

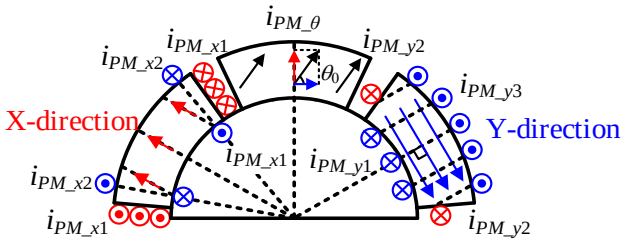

Fig. 2 The equivalence between surface current and Halbach PM array in the Cartesian coordinate.

For the Y-direction, the surface currents along the inner surface of PM are obtained from the length of magnetization.

$$i_{PM\_y1}(R_r,\alpha_{PM})=\frac{2H_{cj}R_r\sin(\frac{\alpha_0}{2})}{n_{PM\_t}} \tag{7}$$

Similarly, the outer surface currents of PM corresponding to the inner surface in parallel have similar expression, while the other part of outer surface currents should be paired with the surface current along the PM sides. They can be expressed as

$$\begin{aligned} i_{PM\_y2}(r_{PM},\alpha_{PM1}) &= i_{PM\_y2}(r_{PM},\alpha_{PM2}) \\ &= \frac{H_{cj}R_m\alpha_{\triangle}}{n_{PM\_r}}\sin\left(\frac{\alpha_0}{2}\right) \end{aligned} \tag{8}$$

$$i_{PM\_y3}(R_m,\alpha_{PM})=\begin{cases} i_{PM\_y2}(r_{PM},\alpha_{PM1}),\alpha_{PM1}\le\alpha_{PM}<\alpha_{PM1}+\alpha_{\triangle} \\ i_{PM\_y1}(R_r,\alpha_{PM}),\alpha_{PM1}+\alpha_{\triangle}\le\alpha_{PM}<\alpha_{PM2}-\alpha_{\triangle} \\ i_{PM\_y2}(r_{PM},\alpha_{PM2}),\alpha_{PM2}-\alpha_{\triangle}\le\alpha_{PM}\le\alpha_{PM2} \end{cases} \tag{9}$$

where $\alpha_{\Delta}=\alpha_0/2-\arcsin[R_r/R_m\cdot\sin(\alpha_0/2)]$. Then, the Halbach PM array with different magnetization directions based on Cartesian coordinate can be calculated from (5)-(9) for the current values while the positions of the surface current stay unchanged.

$$\begin{aligned} i_{PM\_\theta}(r_{PM},\alpha_{PM1}) = \frac{H_{cj}}{n_{PM\_r}}\Bigg[& h_m\sin\left(\frac{\alpha_0}{2}\right)\cos(\theta_0)+ \\ & R_m\alpha_{\triangle}\cos\left(\frac{\alpha_0}{2}\right)\sin(\theta_0)\Bigg] \end{aligned} \tag{10}$$

$$\begin{aligned} i_{PM\_\theta}(r_{PM},\alpha_{PM2}) = \frac{H_{cj}}{n_{PM\_r}}\Bigg[& R_m\alpha_{\triangle}\sin\left(\frac{\alpha_0}{2}\right)\cos(\theta_0)- \\ & h_m\cos\left(\frac{\alpha_0}{2}\right)\sin(\theta_0)\Bigg] \end{aligned} \tag{11}$$

$$\begin{aligned} i_{PM\_\theta}(R_r,\alpha_{PM}) = \frac{H_{cj}R_r}{n_{PM\_t}}\Bigg[& \alpha_0\sin\left(\alpha_{PM}-\frac{\alpha_{PM1}+\alpha_{PM2}}{2}\right)\sin(\theta_0)+ \\ & 2\sin(\frac{\alpha_0}{2})\cos(\theta_0)\Bigg] \end{aligned} \tag{12}$$

$$\begin{aligned} i_{PM\_\theta}(R_m,\alpha_{PM}) = & -\frac{H_{cj}R_r\alpha_0}{n_{PM\_t}}\sin\left(\alpha_{PM}-\frac{\alpha_{PM1}+\alpha_{PM2}}{2}\right)\sin(\theta_0) \\ & -i_{PM\_y3}(R_m,\alpha_{PM})\bullet\cos(\theta_0) \end{aligned} \tag{13}$$

Hence, the matrix form of the surface current for the Halbach PM array can be expressed as

$$\begin{aligned} \mathbf{I_{PM}}(\mathbf{r_{PM}},\boldsymbol{\alpha}_{\mathbf{PM}},t) &= \begin{bmatrix} i_{PM\_\theta}(R_m,\alpha_{PM}) \\ i_{PM\_\theta}(R_r,\alpha_{PM}) \\ i_{PM\_\theta}(r_{PM},\alpha_{PM2}) \\ i_{PM\_\theta}(r_{PM},\alpha_{PM1}) \\ \vdots \end{bmatrix} \\ &= \begin{bmatrix} i_{PM\_\theta}(r_k,wt+\alpha_k) & \cdots \end{bmatrix}^{\mathrm{T}} \end{aligned} \tag{14}$$

where w is the rotational speed of the motor. r_k and α_k represent the initial position of the surface current in the polar coordinate. For example, $\alpha_{PM}=wt+\alpha_1$, $\alpha_{PM2}=wt+\alpha_2$, $\alpha_{PM1}=wt+\alpha_3$, where k=1,2,3, respectively.

The winding currents are located at $(\mathbf{r_{sc}},\boldsymbol{\alpha}_{\mathbf{sc}})$ in the slot region, and the current values are calculated using the input phase current and number of turns, which is expressed as

$$\mathbf{I_{wc}}(\mathbf{r_{sc}},\boldsymbol{\alpha}_{\mathbf{sc}},t)=i_m N_t\mathbf{M_s}\begin{bmatrix} \sin(pwt+\theta_e) \\ \sin(pwt+\theta_e+\frac{2}{3}\pi) \\ \sin(pwt+\theta_e-\frac{2}{3}\pi) \end{bmatrix} \tag{15}$$

where i_m is the phase current amplitude, N_t is the number of turns per slot, and p is the number of pole pairs. $\mathbf{M_s}$ represents the matrix form of winding configuration to transform the phase current into the slot current distribution.

Once the equivalent currents representing PMs and winding current are obtained, the air-gap field of QHAPMSM can be analytically calculated using the conformal mapping technique considering the slotting effect. The conformal mapping function can transform the slotted air gap of the S domain to the slotless annulus of ψ domain using the following equation [18]:

$$S=r_s e^{j\alpha_s}=e^{Z} \tag{16}$$

$$Z=A_0\int\prod_{k=1}^{n-1}(W-w_k)^{-\frac{\beta_k}{\pi}}dW+C_0 \tag{17}$$

$$W=\frac{\Delta x}{2\pi}\left(\pi+j\log(r_\psi)-\alpha_\psi\right)+j\frac{\Delta y}{2} \tag{18}$$

where the parameters of (16)-(18) are obtained from the total region, including the rotor shaft, PM, air gap, and slot dimension. As the rotor iron is removed in the Halbach array PM motors, theoretically, there is no boundary condition along the inner radius of the total region and no rotor iron saturation. However, to avoid the singular values in the analytical calculation, this paper assumes that the radius of the inner boundary is ten times smaller than the inner radius of the magnet, which only introduces minor errors in calculating the air-gap field.

Then, the magnetic field at the position (r_ψ,α_ψ) of slotless ψ domain can be calculated from the equivalent current i_{eqk} at the position $(R_{c\psi},\alpha_{c\psi})$ using (16)-(18) [29]:

$$\begin{aligned} B_{r\psi k}\left(r_\psi,\alpha_\psi\right) = & \frac{\mu_0 i_{eqk}(R_{c\psi},\alpha_{c\psi})}{2\pi}\Bigg\{\sum_{n=1}^{\infty}\frac{R_{s\psi}^n}{R_{c\psi}^n}\Bigg(\frac{R_{s\psi}^{2n}+R_{c\psi}^{2n}}{R_{r\psi}^{2n}-R_{s\psi}^{2n}}\cdot \\ & \frac{r_\psi^{n-1}}{R_{s\psi}^n}+\frac{R_{c\psi}^{2n}+R_{r\psi}^{2n}}{R_{r\psi}^{2n}-R_{s\psi}^{2n}}\cdot\frac{R_{s\psi}^n}{r_\psi^{n+1}}\Bigg)\sin\left[n\left(\alpha_\psi-\alpha_{c\psi}\right)\right]+\delta_\psi\Bigg\} \end{aligned} \tag{19}$$

$$\begin{aligned} B_{t\psi k}\left(r_\psi,\alpha_\psi\right) = & \frac{\mu_0 i_{eqk}(R_{c\psi},\alpha_{c\psi})}{2\pi r_\psi}\Bigg\{\sum_{n=1}^{\infty}\frac{R_{s\psi}^n}{R_{c\psi}^n}\Bigg(\frac{R_{s\psi}^{2n}+R_{c\psi}^{2n}}{R_{r\psi}^{2n}-R_{s\psi}^{2n}}\cdot \\ & \frac{r_\psi^{\,n}}{R_{s\psi}^n}-\frac{R_{c\psi}^{2n}+R_{r\psi}^{2n}}{R_{r\psi}^{2n}-R_{s\psi}^{2n}}\cdot\frac{R_{s\psi}^n}{r_\psi^{\,n}}\Bigg)\cos\left[n\left(\alpha_\psi-\alpha_{c\psi}\right)\right]+\gamma_\psi\Bigg\} \end{aligned} \tag{20}$$

where $R_{s\psi}$ and $R_{r\psi}$ are the outer and inner radii of the annulus in ψ domain. Next, the radial and tangential component of air-gap field B_{rsk} and B_{tsk} at the position (r_{sk},α_{sk}) of S domain can be obtained from $B_{r\psi k}(r_\psi,\alpha_\psi)$ and $B_{t\psi k}(r_\psi,\alpha_\psi)$ in the ψ domain using the conformal mapping function.

$$B_{rsk}+jB_{tsk}=\left(B_{r\psi k}+jB_{t\psi k}\right)\left(\frac{\partial\psi}{\partial W}\right)^*\left(\frac{\partial Z}{\partial W}\right)^*\left(\frac{\partial Z}{\partial S}\right)^* \tag{21}$$

where $\frac{\partial \psi}{\partial W}$, $\frac{\partial Z}{\partial W}$ and $\frac{\partial Z}{\partial S}$ are calculated from (16)-(18). Then, the air-gap field produced by the Halbach PM array and winding current can be expressed as

$$\begin{aligned} B_{r\_inf} &= \sum_k B_{rsk}(r_{sk}, a_{sk}) = \mathbf{g_1}(\mathbf{I_{PM}}(t)) + \mathbf{g_2}(\mathbf{I_{wc}}(t)) \\ B_{t\_inf} &= \sum_k B_{tsk}(r_{sk}, a_{sk}) = \mathbf{h_1}(\mathbf{I_{PM}}(t)) + \mathbf{h_2}(\mathbf{I_{wc}}(t)) \end{aligned} \tag{22}$$

where $\mathbf{g_1}$, $\mathbf{g_2}$, $\mathbf{h_1}$, and $\mathbf{h_2}$ are the matrix function and they are derived from (19)-(21). The relationship between the air-gap field and the current value is linear, while it is more complicated to show the influence of the current position on the air-gap field due to the process of conformal mapping using (16)-(18). Nevertheless, the coefficients in the conformal mapping are determined as long as the motor dimension is given. Hence, the mathematical relationship between the air-gap field and motor dimension is obtained when neglecting iron saturation.

B. *Magnetic Circuit Model for Stator Iron*

The magnetic field of stator iron in the QHAPMSM is calculated using the magnetic circuit model in Fig. 3. The stator yoke, tooth body, and tooth tip are all represented using the nonlinear magnetic reluctances. The flux source from the air gap and slot $\mathbf{\Psi_s}$ are calculated from the LAM at first, where $\mathbf{\Psi_s}$ =[ψ_{s1}, ψ_{s2}, …] in Fig. 3. The modular and parameterized magnetic circuit can be extended to represent the stator region with any slot number, Fig. 3. According to the Kirchhoff's voltage law, the magnetic potential distribution $\mathbf{V_s}$ in the magnetic circuit model can be calculated using

$$\mathbf{V_s} = \left(\mathbf{E}\mathbf{G_s}\mathbf{E}^{\mathrm{T}}\right)^{-1}\mathbf{\Psi_s} \tag{23}$$

where $\mathbf{E}$ and $\mathbf{G_s}$ are the incidence matrix and magnetic permeance, respectively. It is noted that $\mathbf{G_s}$ builds the nonlinear relationship between the iron permeance and flux density in the stator.

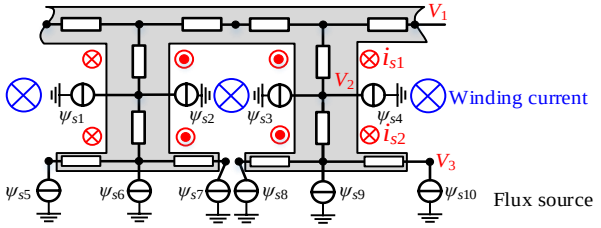

Fig. 3 The magnetic circuit model of the stator to consider iron saturation.

The iron saturation is represented by the magnetic potential drop in the stator. It is transformed to the equivalent saturation current in the LAM to account for saturation.

$$\begin{cases} i_{s1} = V_1 - V_2 \\ i_{s2} = V_2 - V_3 \end{cases} \tag{24}$$

The matrix form of (24) is expressed as

$$\mathbf{I_s} = \mathbf{C_i}\mathbf{V_s} \tag{25}$$

where $\mathbf{I_s}$=[i_{s1}, i_{s2},…], $\mathbf{V_s}$=[V_1,V_2,V_3,…], as shown in Fig. 3. $\mathbf{C_i}$ is the constant matrix from (24). Then, the air-gap field produced by the equivalent saturation current can be calculated as

$$\begin{aligned} B_{r\_sat} &= \mathbf{g_3}(\mathbf{V_s}) \\ B_{t\_sat} &= \mathbf{h_3}(\mathbf{V_s}) \end{aligned} \tag{26}$$

where $\mathbf{g_3}$ and $\mathbf{h_3}$ are the matrix function between the air-gap flux density and the magnetic potential distribution, which are derived from (19)-(21) and (25). Hence, the $\mathbf{\Psi_s}$ will be updated in the following steps to obtain the convergent value of $\mathbf{I_s}$, which is presented in the following subsection.

C. *Field Separation Theory for Motor Performance*

According to the FST, the radial and the tangential component of the total air-gap field B_{rs}, B_{ts} can be expressed as

$$\begin{aligned} B_{rs} &= \mathbf{g_1}(\mathbf{I_{PM}}(t)) + \mathbf{g_2}(\mathbf{I_{wc}}(t)) + \mathbf{g_3}(\mathbf{V_s}) \\ B_{ts} &= \mathbf{h_1}(\mathbf{I_{PM}}(t)) + \mathbf{h_2}(\mathbf{I_{wc}}(t)) + \mathbf{h_3}(\mathbf{V_s}) \end{aligned} \tag{27}$$

It gives the mathematical relationship between the saturated air-gap field and motor dimension via $\mathbf{g_1}$, $\mathbf{g_2}$, $\mathbf{g_3}$, $\mathbf{h_1}$, $\mathbf{h_2}$, and $\mathbf{h_3}$.

To improve the accuracy of the magnetic field prediction, the flux source $\mathbf{\Psi_s}$ in Fig. 3 should be updated by including the equivalent saturation field in the iteration. Therefore, $\mathbf{V_s}$ is modified using (23) to account for the iron saturation and a new prediction of the magnetic field is obtained using (27) with better accuracy. After several iterations, the convergent value of $\mathbf{V_s}$ is determined, as well as the air-gap field distribution considering iron saturation. The iterative solving process for calculating the equivalent saturation current is shown in the second green box of Fig. 4. When the flux source $\mathbf{\Psi_s}$ is obtained from the LAM in the first green box of Fig. 4, the magnetic potential distribution $\mathbf{V_s}(k)$ is calculated using (23) at k^{th} step. Meanwhile, the magnetic field strength of the reluctances is calculated from $\mathbf{V_s}(k)$, and then the nonlinear BH curve of the iron is employed to determine the permeability of the magnetic reluctances (i.e., $\mathbf{G_s}$) in the magnetic circuit. After updating $\mathbf{G_s}$ and $\mathbf{\Psi_s}$, the new value of $\mathbf{V_s}(k+1)$ is calculated again using (23) for the next $(k+1)^{\mathrm{th}}$ step. This iterative calculation will be stopped if it reaches the convergence criteria in Fig. 4.

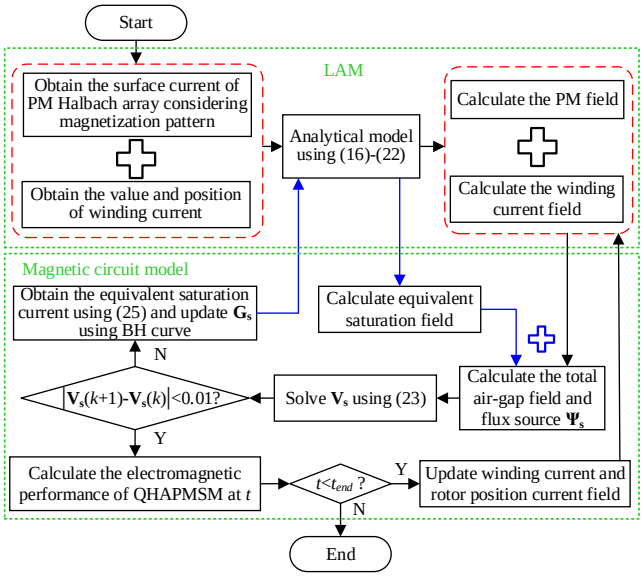

Fig. 4 The flowchart of calculating the equivalent current of saturation.

Then, according to the solution of the slotted air-gap field in (27), the electromagnetic torque of QHAPMSM is calculated using

$$T_c = \frac{l_e}{\mu_0} r^2 \int_0^{2\pi} B_{rs} B_{ts} d\alpha \tag{28}$$

where r is the radius of the path for predicting the air-gap flux density, and l_e is the effective length. Meanwhile, the flux linkage Ψ_{ABC} of QHAPMSM can be calculated from the air-gap field and winding layout. Hence, the back-EMF is computed using

$$E_{ABC} = -\frac{d\psi_{ABC}}{dt} \tag{29}$$

III. Finite Element Validation

An 8-pole/9-slot QHAPMSM is designed and built to show the effectiveness of the proposed method. The permeability of stator iron is nonlinear, as given in Fig. 5. Due to the special flux path of the Halbach array, the iron of the rotor yoke is removed, and therefore, the PMs are stuck on the non-magnetic shaft. The FEM with different magnetization patterns is carried out using commercial software in Fig. 6. The main parameters of QHAPMSM are given in Table I. It is noted that the manufacture of PMs with parallel magnetization (Machine II) is easier and cheaper than that with radial and tangential magnetization (Machine I). Therefore, it is used for the prototype motor. The test rig of QHAPMSM is used to measure the voltage and torque of the prototype, as shown in Fig. 7. The FEM and experimental results are compared with the analytical calculations to validate the high computational speed and accuracy of the proposed model.

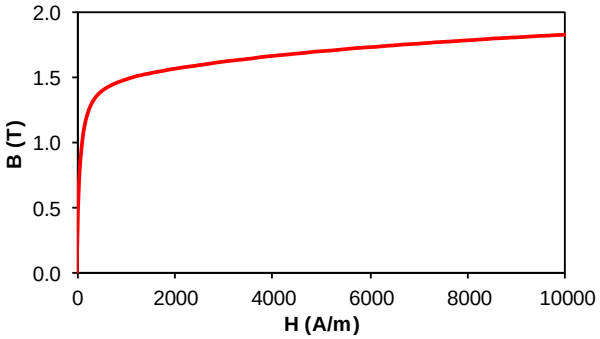

Fig. 5 BH curve of stator iron in the 8-pole/9-slot QHAPMSM.

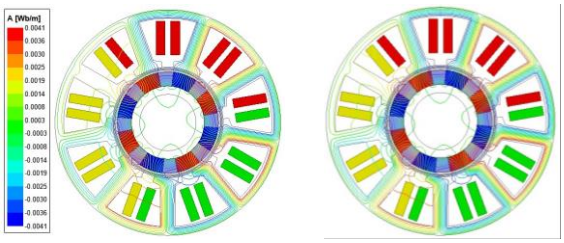

(a) (b)

Fig. 6 The flux density distribution 8-pole/9-slot QHAPMSM using actual electrical steel under on-load conditions: (a) Machine I, (b)Machine II.

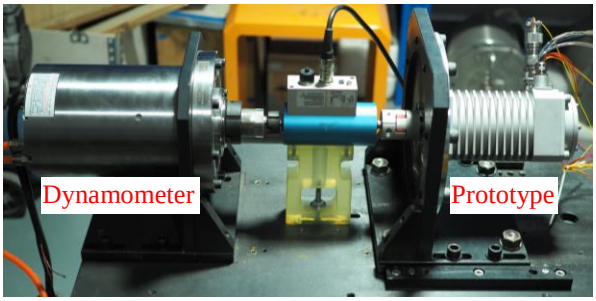

Fig. 7 The test rig for the performance of QHAPMSM.

TABLE I
Main Parameters of QHAPMSM

Parameter	Value	Parameter	Value
Stator diameter	80mm	Rotor diameter	35.8mm
Shaft diameter	25.8mm	Magnet height	5mm
Slot-opening	4.3mm	Tooth width	5.3mm

The on-load air-gap field of QHAPMSM is obtained using FST, and the predictions are compared with FEM results in Figs. 8-9, which shows excellent accuracy. It is noted that FEM-non represents that the iron permeability of QHAPMSM in the FEM is nonlinear, as shown in Fig. 5, while FEM-inf means that the iron permeability is assumed infinite. Fig. 9(a) shows that the radial flux density of Machine II in the air gap at 120 degree exhibits some differences with and without magnetic saturation, while they are similar for Machine I in Fig. 8(a). Hence, it can be concluded that the iron saturation of Machine II with parallel magnetization is more severe than Machine I with radial and tangential magnetization from Figs. 8-9.

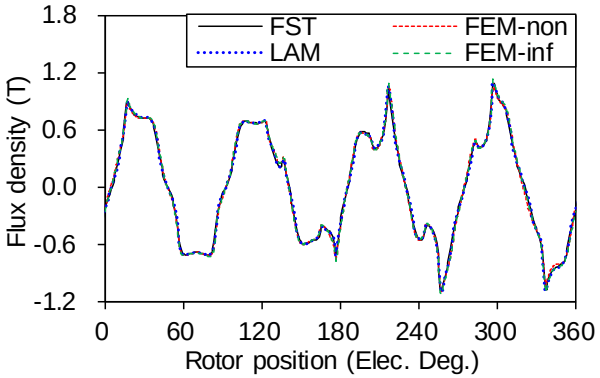

(a) radial component

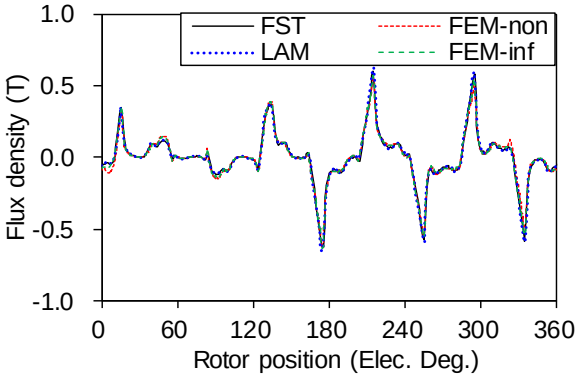

(b) tangential component

Fig. 8 The calculated air-gap field distribution under on-load condition for Machine I.

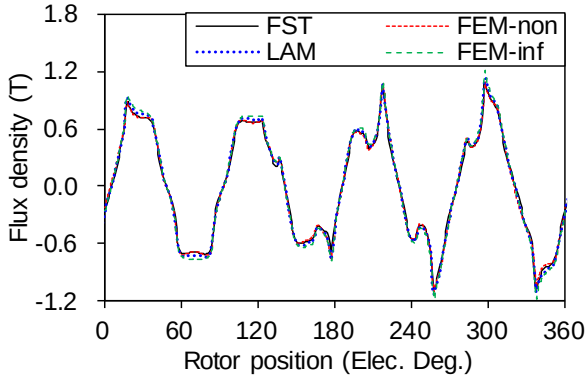

(a) radial component

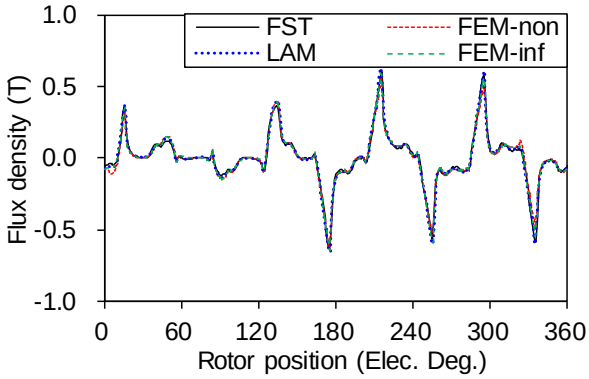

(b) tangential component

Fig. 9 The calculated air-gap field distribution under on-load conditions for Machine II.

Then, the harmonic analysis of the air-gap field at different currents is performed to show the effectiveness of the FST. For the main harmonic flux density (4th order), the radial component is slightly influenced by the current. The average error of FST at different currents for the 4th order harmonic amplitude of the radial flux density is 1.9% and 2.5% in Machine I and Machine II, respectively. The 5th order harmonic flux density increases in both directions when the current increases for both motors, even though the amplitude is low compared with the 4th order harmonic. In Figs. 10-11, the FST predictions agree well with the FEM-non results, while the LAM calculations are close to the FEM-inf results. It is noted that the differences between LAM and FST show that the iron saturation will decrease the value of 5th order harmonic flux density for both motors.

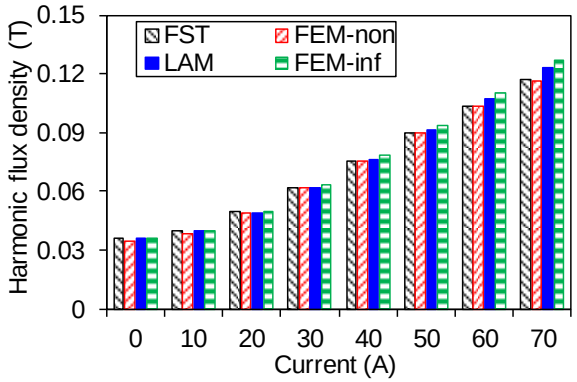

Fig. 10 The relationship between the 5th order harmonic amplitude of the radial flux density and current value for Machine I.

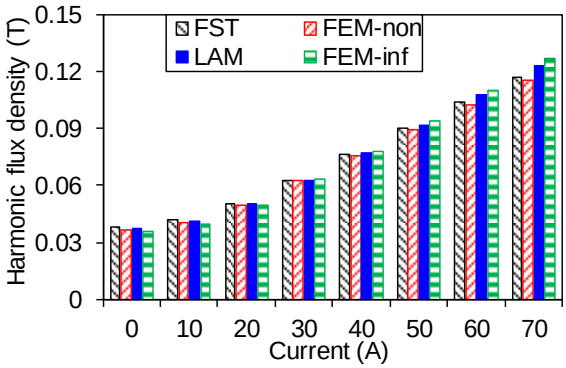

Fig. 11 The relationship between the 5th order harmonic amplitude of the radial flux density and current value for Machine II.

The open-circuit back-EMF predictions using FST agree well with the FEM prediction in Figs. 12-13. The fundamental voltages from the analytical prediction at different loads show high accuracy, Figs. 14-15. When the current increases, the iron saturation will be more severe. The fundamental induced voltage of QHAPMSM can be significantly decreased due to the saturation effect compared with infinite FEM results. For the load torque in Figs. 16-17, the average torque is also reduced when the input current is large, considering iron saturation. The FST calculation agrees well with the nonlinear FEM result. Such errors mainly come from simplifying the magnetic circuit model for the iron region. The infinite FEM with infinitely permeable iron is introduced and compared with nonlinear FEM to show the saturation effect. Figs. 18-19 show the average torque of motors at different currents, which means different saturation levels. The average torque error of FST calculation at different currents is 0.5% and 1.2% for Machine I and Machine II, respectively.

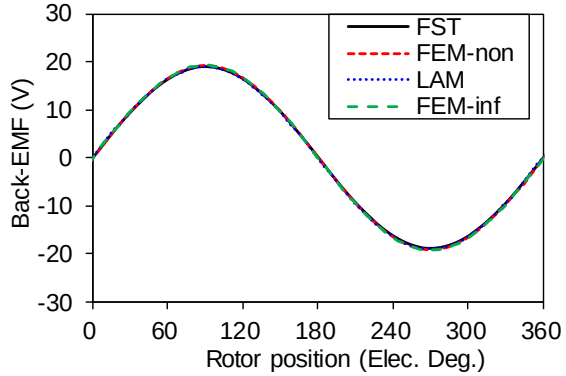

Fig. 12 The calculated back-EMF waveform under open-circuit condition for Machine I.

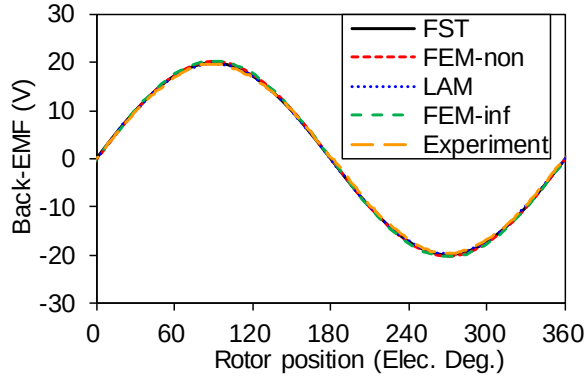

Fig. 13 The calculated and measured back-EMF waveform under open-circuit condition for Machine II.

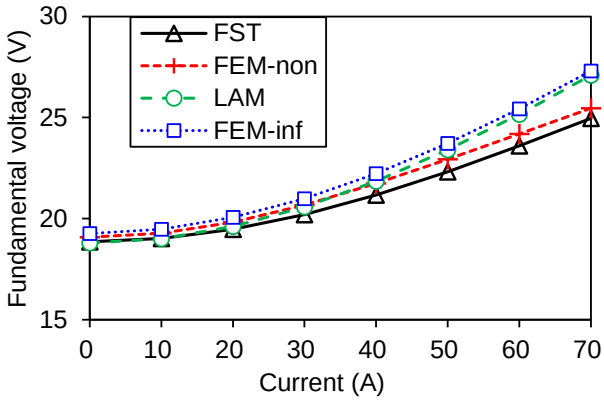

Fig. 14 The relationship between the fundamental induced voltage and current for Machine I.

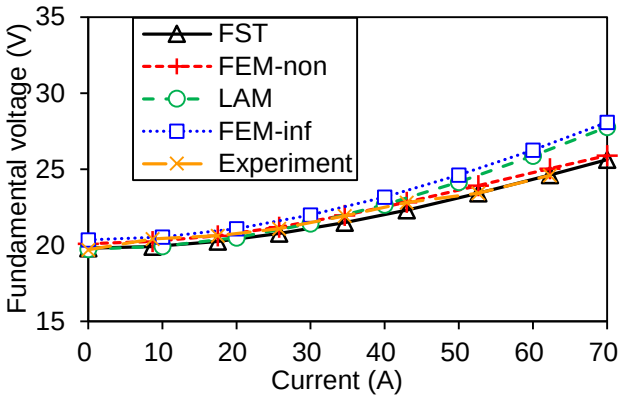

Fig. 15 The relationship between the fundamental induced voltage and current for Machine II.

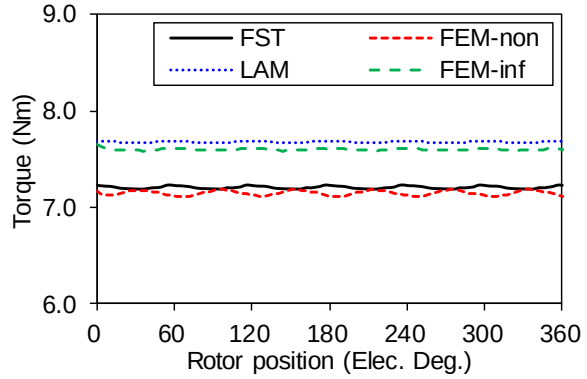

Fig. 16 The calculated on-load torque waveform for Machine I.

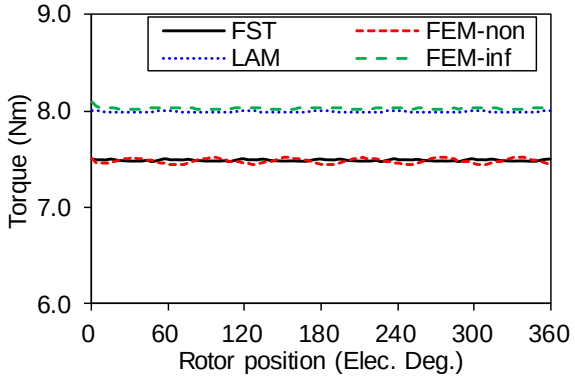

Fig. 17 The calculated on-load torque waveform for Machine II.

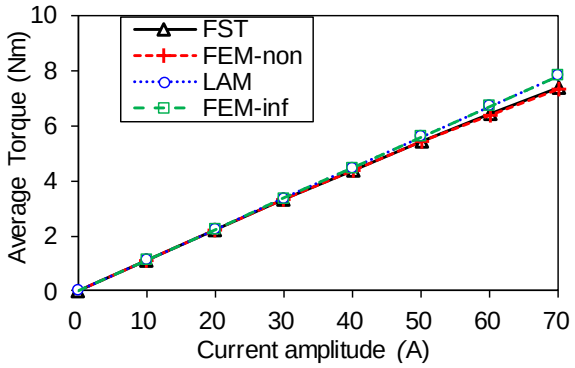

Fig. 18 The relationship between the average torque and current for Machine I.

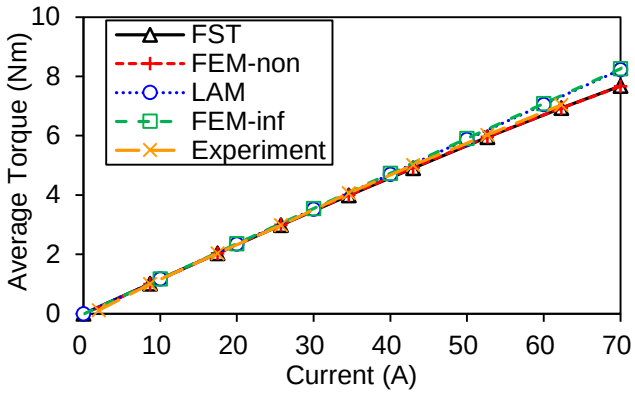

Fig. 19 The relationship between the average torque and current for Machine II.

The number of mesh nodes using FEM is 42533 for both motors. In the FST, the magnetic circuit nodes are 81 for both motors and the number of harmonics in both analytical models is 70. It is noted that coarse mesh will save some time for FEM, but it is not suitable to reduce the mesh node number in the air-gap and PM region, as it could significantly affect the calculation accuracy. Nevertheless, there are always a large number of mesh nodes in these regions, which significantly affects the calculation speed of FEM. The calculation time of QHAPMSM using FST and FEM is given in Table II. The variation of winding current has a small influence on the calculation time as it only increases a few steps of iteration to calculate the iron permeability. FST can save over 4/5 times the calculation time of FEM with excellent accuracy, showing that FST has a significant advantage over FEM in calculation efficiency.

TABLE II
Calculation Time of Machine I and Machine II

Name	Current (A)	0	10	30	50	70
Machine I	LAM (s)	23.8	24.5	24.6	25.1	25.2
	FST (s)	28.5	28.5	28.6	29.0	29.7
	FEM-inf (s)	250	251	268	277	285
	FEM-non (s)	294	302	307	310	311
Machine II	LAM (s)	34.2	34.2	34.4	34.8	35.6
	FST (s)	37.7	38.2	39.4	41.5	41.6
	FEM-inf (s)	230	232	238	243	244
	FEM-non (s)	343	348	351	359	363

The main difference between these two motors is the magnetization direction of PMs. Based on the proposed model, the PM field, winding current field, and equivalent saturation field for both motors are predicted and compared in Fig. 20. It can be seen that the PMs in Machine I contribute to less amplitude of the 4th harmonic field than that in Machine II, due to the different magnetization pattern. Fig. 21 illustrates the magnetic field produced by the primary and auxiliary magnet for both four-pole motors. The auxiliary PMs with tangential magnetization produce less 4th harmonic field than that with parallel magnetization, making Machine I less competitive. However, the primary PMs with radial magnetization produce slightly larger 4th harmonic field than that with parallel magnetization, which gives guidelines for the optimization of the QHAPMSM in the future.

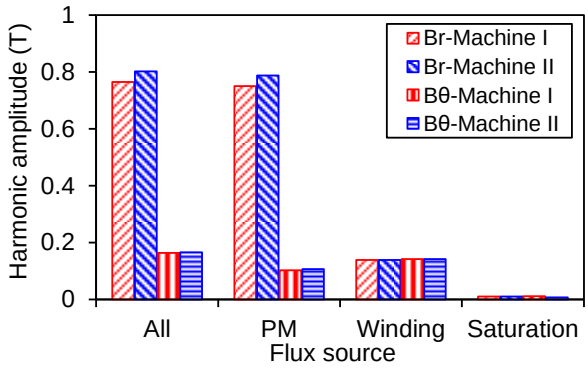

(a) Amplitude

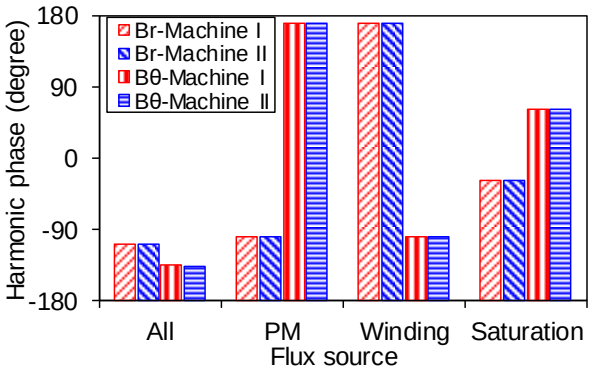

(b) Phase

Fig. 20 The comparison of the 4th harmonic flux density for both motors based on FST at the largest current.

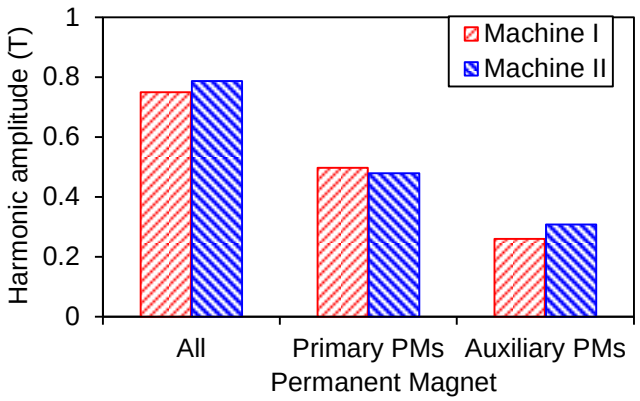

Fig. 21 The 4th harmonic amplitude of the PM field for both motors based on FST at the largest current.

IV. Conclusion

This paper introduces the FST for calculating the performance of QHAPMSM considering both magnetization pattern and saturation effect. It combines the advantages of the conformal mapping model with the magnetic circuit model to significantly improve both calculation accuracy and calculation efficiency. In the conformal mapping model, the equivalent PM current for different magnetization patterns is introduced to represent the magnetization direction in either polar or Cartesian coordinates. The equivalent saturation current is obtained from the magnetic circuit model to show the saturation level in the iron region. A solving loop is required to calculate the nonlinear value of the equivalent saturation current. Based on the FST, the contribution of the different components in the QHAPMSM (i.e., PM, winding, and iron saturation) is investigated and compared for further improvement of motor performance. The FEM and experimental results validate the excellent accuracy and high efficiency of FST.

References

[1] Z. Song, C. Liu, K. Feng, H. Zhao, and J. Yu, "Field prediction and validation of a slotless segmented-Halbach permanent magnet synchronous machine for more electric aircraft," *IEEE Trans. Transport. Electrific.*, vol. 6, no. 4, pp. 1577–1591, Dec. 2020.

[2] R. P. Praveen, M. H. Ravichandran, V. T. Sadasivan Achari, V. P. Jagathy Raj, G. Madhu, and G. R. Bindu, "A novel slotless Halbach-array permanent-magnet brushless dc motor for spacecraft applications," *IEEE Trans. Ind. Electron.*, vol. 59, no. 9, pp. 3553–3560, Sep. 2012.

[3] M. W. Zouaghi, I. Abdennadher, and A. Masmoudi, "No-load features of T-LSMs with quasi-Halbach magnets: application to free piston engines," *IEEE Trans. Energy Convers.*, vol. 31, no. 4, pp. 1591-1600, Dec. 2016.

[4] L. Jing, W. Tang, T. Wang, T. Ben, and R. Qu, "Performance analysis of magnetically geared permanent magnet brushless motor for hybrid electric vehicles," *IEEE Trans. Transport. Electrific.*, vol. 8, no. 2, pp. 2874-2883, June 2022.

[5] L. Jing, W. Liu, W. Tang, and R. Qu, "Design and optimization of coaxial magnetic gear with double-layer PMs and spoke structure for tidal power generation," *IEEE/ASME Trans. Mechatron.*, 2023, in press.

[6] K. Liu, M. Yin, W. Hua, Z. Ma, M. Lin, and Y. Kong, "Design and analysis of Halbach ironless flywheel BLDC motor/generators," *IEEE Trans. Magn.*, vol. 54, no. 11, pp. 1–5, Nov. 2018.

[7] C. Shi, D. Li, R. Qu, H. Zhang, Y. Gao, and Y. Huo, "A novel linear permanent magnet vernier machine with consequent-pole permanent magnets and Halbach permanent magnet arrays," *IEEE Trans. Magn.*, vol. 53, no. 11, pp. 1–4, Nov. 2017.

[8] Q. Chen, Y. Fan, Y. Lei, and X. Wang, "Multiobjective optimization design of unequal Halbach array permanent magnet vernier motor based

on optimization algorithm," *IEEE Trans. Ind. Appl.*, vol. 58, no. 5, pp. 6014–6023, Sep. 2022.

[9] L. Xu, X. Zhu, C. Zhang, L. Zhang, and L. Quan, "Power oriented design and optimization of dual stator linear-rotary generator with Halbach PM array for ocean energy conversion," *IEEE Trans. Energy Convers.*, vol. 36, no. 4, pp. 3414–3426, Dec. 2021.

[10] B. Koo, J. Kim and K. Nam, "Halbach array PM machine design for high speed dynamo motor," *IEEE Trans. Magn.*, vol. 57, no. 2, pp. 1-5, Feb. 2021.

[11] S. Wu, X. Zhao, Z. Jiao, P. Luk, and C. Jiu, "Multi-objective optimal design of a toroidally wound radial-flux Halbach permanent magnet array limited angle torque motor," *IEEE Trans. Ind. Electron.*, vol. 64, no. 4, pp. 2962–2971, Apr. 2017.

[12] A. Rahideh, A. Ghaffari, A. Barzegar, and A. Mahmoudi, "Analytical model of slotless brushless pm linear motors considering different magnetization patterns," *IEEE Trans. Energy Convers.*, vol. 33, no. 4, pp. 1797–1804, Dec. 2018.

[13] M. Markovic and Y. Perriard, "Optimization design of a segmented Halbach permanent-magnet motor using an analytical model," *IEEE Trans. Magn.*, vol. 45, no. 7, pp. 2955–2960, Jul. 2009.

[14] Y. Ni, Z. Liu, B. Xiao, and Q. Wang, "Optimum split ratio in surface-mounted permanent magnet machines with pieced Halbach magnet array," *IEEE Trans. Energy Convers.*, vol. 35, no. 4, pp. 1877–1885, Dec. 2020.

[15] M. W. Zouaghi, I. Abdennadher, and A. Masmoudi, "No-load features of T-LSMs with quasi-Halbach magnets: application to free piston engines," *IEEE Trans. Energy Convers.*, vol. 31, no. 4, pp. 1591–1600, Dec. 2016.

[16] H. S. Zhang, Z. X. Deng, M. L. Yang, Y. Zhang, J. Y. Tuo, and J. Xu, "Analytical prediction of Halbach array permanent magnet machines considering finite tooth permeability," *IEEE Trans. Magn.*, vol. 56, no. 6, pp. 1–10, Jun. 2020.

[17] L. Wu, H. Yin, D. Wang, and Y. Fang, "On-load field prediction in SPM machines by a subdomain and magnetic circuit hybrid model," *IEEE Trans. Ind. Electron.*, vol. 67, no. 9, pp. 7190–7201, Sep. 2020.

[18] A. Hanic, D. Zarko, D. Kuhinek, and Z. Hanic, "On-load analysis of saturated surface permanent magnet machines using conformal mapping and magnetic equivalent circuits," *IEEE Trans. Energy Convers.*, vol. 33, no. 3, pp. 915–924, Sep. 2018.

[19] P. Liang, F. Chai, Y. Yu, and L. Chen, "Analytical model of a spoke-type permanent magnet synchronous in-wheel motor with trapezoid magnet accounting for tooth saturation," *IEEE Trans. Ind. Electron.*, vol. 66, no. 2, pp. 1162–1171, Feb. 2019.

[20] S. Li, W. Tong, S. Wu and R. Tang, "Analytical model for electromagnetic performance prediction of ipm motors considering different rotor topologies," *IEEE Trans. Ind. Appl.*, 2023, in press.

[21] Z. Li, X. Huang, L.J. Wu, H. Zhang, T.N. Shi, Y. Yan, B. Shi, and G. Yang, "An improved hybrid field model for calculating on-load performance of interior permanent-magnet motors," *IEEE Trans. Ind. Electron.*, vol. 68, no. 10, pp. 9207–9217, 2021.

[22] Y. Du, Y. Huang, B. Guo, F. Peng, and J. Dong, "Semi-analytical model of multi-phase Halbach array axial flux permanent-magnet motor considering magnetic saturation," *IEEE Trans. Transport. Electrific.*, 2022, in press.

[23] Y. Oner, Z. Q. Zhu, L. J. Wu, X. Ge, H. Zhan, and J. T. Chen, "Analytical on-load subdomain field model of permanent-magnet vernier machines," *IEEE Trans. Ind. Electron.*, vol. 63, no. 7, pp. 4105-4117, Jul. 2016.

[24] J. Zhu, Y. Fan, H. Chen, J. Chen, Y. Zuo, and C. H. T. Lee, "Comprehensive armature reaction modeling and flux weakening optimization of a surface permanent magnet vernier motor," *IEEE Trans. Ind. Electron.*, vol. 70, no. 9, pp. 8709-8722, Sept. 2023.

[25] L. Fang, D. Li, and R. Qu, "Torque improvement of vernier permanent magnet machine with larger rotor pole pairs than stator teeth number," *IEEE Trans. Ind. Electron.*, vol. 70, no. 12, pp. 12648-12659, Dec. 2023.

[26] J. Zhu, Y. Zuo, H. Chen, J. Chen, and C. H. T. Lee, "Deep-investigated analytical modeling of a surface permanent magnet vernier motor," *IEEE Trans. Ind. Electron.*, vol. 69, no. 12, pp. 12336-12347, Dec. 2022.

[27] Z. Li, X. Huang, A. Liu, Z. Liu, L. Wu, and T. Shi, "Analytical model of electromagnetic performance for permanent-magnet vernier machines using nonlinear exact conformal model", *IEEE Trans. Transport. Electrific.*, vol. 8, no. 2, pp. 2005-2014, June 2022.

[28] F. Zhao, K. Yang, C. Zhang, and L. Li, "Analytical prediction of the flux reversal permanent magnet machine with Halbach array magnets in rotor slot considering saturation", *IET Renew. Power Gener.*, vol. 16, no. 8, pp. 1562–1576, 2022.

[29] Z. Li, X. Huang, L. Wu, T. Long, B. Shi, and H. Zhang, "Open-circuit field prediction of interior permanent-magnet motor using hybrid field model accounting for saturation," *IEEE Trans. Magn.*, vol. 55, no. 7, pp. 1–7, Jul. 2019.